

A STUDY OF RADIO POLARIZATION IN PROTOSTELLAR JETS

MARIANA CÉCERE^{1,5}, PABLO F. VELÁZQUEZ², ANABELLA T. ARAUDO³, FABIO DE COLLE²,
ALEJANDRO ESQUIVEL², CARLOS CARRASCO-GONZÁLEZ⁴, AND LUIS F. RODRÍGUEZ⁴

Draft version July 9, 2021

ABSTRACT

Synchrotron radiation is commonly observed in connection with shocks of different velocities, ranging from relativistic shocks associated with active galactic nuclei, gamma-ray bursts or microquasars to weakly- or non-relativistic flows as those observed in supernova remnants. Recent observations of synchrotron emission in protostellar jets are important not only because they extend the range over which the acceleration process works, but also because they allow to determine the jet and/or interstellar magnetic field structure, thus giving insights on the jet ejection and collimation mechanisms. In this paper, we compute for the first time polarized (synchrotron) and non polarized (thermal X-ray) synthetic emission maps from axisymmetrical simulations of magnetized protostellar jets. We consider models with different jet velocities and variability, as well as toroidal or helical magnetic field. Our simulations show that variable, low-density jets with velocities $\sim 1000 \text{ km s}^{-1}$ and ~ 10 times lighter than the environment can produce internal knots with significant synchrotron emission, and thermal X-rays in the shocked region of the leading bow shock moving in a dense medium. While models with a purely toroidal magnetic field show a very large degree of polarization, models with helical magnetic field show lower values and a decrease of the degree of polarization, in agreement with observations of protostellar jets.

Subject headings: Herbig-Haro objects — ISM: jets and outflows — magnetohydrodynamics (MHD) — polarization — radiation mechanisms: non-thermal — shock waves

1. INTRODUCTION

Jets are present in astrophysical sources with various spatial scales, from Young Stellar Objects (YSOs) to active galactic nuclei (AGN). These collimated outflows are generally considered to be the result of bipolar ejection of plasma, associated with accretion onto a central object (Blandford & Payne 1982). Variability in the ejection speed can produce internal shocks clearly seen in YSO jets in the form of bright optical knots (e.g., Raga & Noriega-Crespo 1998; Masciadri et al. 2002) called Herbig-Haro (HH) objects.

Jets that arise from active galaxies can have relativistic speeds, and are well known synchrotron radiation emitters (see for example Tregillis et al. 2001; Laing et al. 2006; Gómez et al. 2008). In contrast, YSO jets are non-relativistic and typically thermal radio sources. However, a few stellar sources, such as Serpens (Rodríguez et al. 1989), HH 80-81 (Martí et al. 1995), Cepheus-A (Garay et al. 1996), W3(OH) (Wilner et al. 1999), and IRAS 16547-4247 (Garay et al. 2003) present radio emission with negative spectral index interpreted as non-thermal (synchrotron) radiation. Notably, polarized radio emission was detected in the jet of HH 80-81 (Carrasco-González et al. 2010). Therefore, an interesting question

to answer is how jets with velocities of several hundreds km s^{-1} moving into a dense medium are able to produce shocks where particles can be accelerated up to relativistic energies and produce synchrotron radio emission.

Synchrotron maps have been computed from MHD numerical simulations by several authors in different contexts such as pulsar wind nebulae, e.g. Del Zanna et al. (2006), Volpi et al. (2008); supernova remnants, e.g. Orlando et al. (2007); and accretion disks, e.g. Goldston et al. (2005). Broderick & McKinney (2010) and Porth et al. (2011) have performed MHD numerical simulations of relativistic jets. In particular, Porth et al. (2011) have performed MHD numerical simulation of relativistic AGN jets in order to study the synchrotron emission at the jet acceleration region by computing synthetic emission maps of the spectral index, polarization degree and Rotation Measure (RM). In the case of non-relativistic (YSO) jets, given the large densities of such a jets at the launching region, the base of the jet is a thermal emitter. However, as the jets propagates the density decreases and non-thermal signatures can appear.

We present a polarization study in order to shed light on the understanding of the non-thermal emission in protostellar jets. We model, by using axisymmetric, magnetohydrodynamic (MHD) simulations, the synchrotron emission, and we compute the resulting polarization map. The paper is organized as follows: in Section 2, we describe the model and the numerical setup; in Section 3 we show the results (synthetic radio, polarization, and X-ray emission maps); and in Section 4 we present our conclusions.

2. NUMERICAL CALCULATIONS

2.1. Initial setup

¹ Instituto de Astronomía Teórica y Experimental, Universidad Nacional de Córdoba, X5000BGR, Córdoba, Argentina

² Instituto de Ciencias Nucleares, Universidad Nacional Autónoma de México, Apdo. Postal 70-543, CP: 04510, D.F., México

³ University of Oxford, Astrophysics, Keble Road, Oxford OX1 3RH, UK

⁴ Instituto de Radioastronomía y Astrofísica, Universidad Nacional Autónoma de México, Apdo. Postal 3-72, 58090, Morelia, Michoacán, México

⁵ Consejo Nacional de Investigaciones Científicas y Técnicas (CONICET), Argentina.

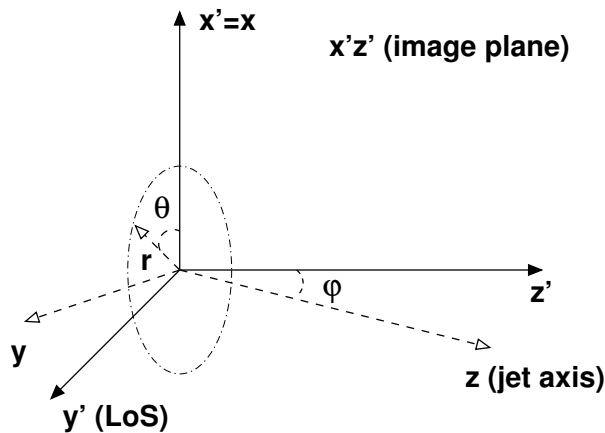


FIG. 1.— Coordinate system employed for simulating synchrotron emission. The rz -plane is the 2D plane of our axisymmetric simulation. The plane of the sky or image plane is the $x'z'$ -plane and the y' -axis is the LoS.

Our study is based on 2.5D axisymmetric, MHD simulations carried out with the adaptive mesh refinement, eulerian code *Mezcal* (De Colle & Raga 2006; De Colle et al. 2008, 2012). We consider a 2D axisymmetrical adaptive grid, with a size of 0.2 and 0.5 pc along the r - and z -directions, respectively, and a maximum spatial resolution of 1.56×10^{-4} pc, corresponding to 1280×3200 cells (at the maximum resolution) along the r - and z -directions, and 6 levels of refinement. The environment in which the jet propagates is homogeneous, with a uniform density $n_{\text{env}} = 3000 \text{ cm}^{-3}$, temperature $T_{\text{env}} = 100 \text{ K}$, and magnetic field B_0 . At every timestep the jet is imposed in the computational domain by rewriting the values of the physical parameters inside a region of the computational domain with $r < R_{\text{jet}} = 0.03 \text{ pc}$ and $z < 0.003 \text{ pc}$, with density $n_{\text{jet}} = 300 \text{ cm}^{-3}$ (Araudó & Rodríguez 2012) and velocity v_{jet} (along the z -axis). The longitudinal magnetic field (imposed on all computational domain) is $B_z = B_0$, and the toroidal component is given by (Lind et al. 1989)

$$B_\phi(r) = \begin{cases} B_m \left(\frac{r}{R_m} \right) & 0 \leq r < R_m; \\ B_m \left(\frac{R_m}{r} \right) & R_m \leq r < R_{\text{jet}}; \\ 0 & r \geq R_{\text{jet}}, \end{cases} \quad (1)$$

where $R_m = 0.02 \text{ pc}$, and B_m is given in Table 1. In models M4 and M5 B_z and B_m are chosen so that B ($= \sqrt{B_z^2 + B_m^2}$) results of the order of 0.1 mG (Carrasco-González et al. 2010; Curran & Chrysostomou 2007). The jet pressure profile is constructed to ensure total pressure equilibrium at $t = 0$:

$$p(r) = \begin{cases} \frac{B_m^2}{8\pi} \left(\beta_m - \frac{r^2}{R_m^2} \right) & 0 \leq r < R_m; \\ \frac{B_m^2}{8\pi} \left(\beta_m - \frac{R_m^2}{r^2} \right) & R_m \leq r < R_{\text{jet}}; \\ p_{\text{env}} & r \geq R_{\text{jet}}, \end{cases} \quad (2)$$

where $\beta_m = p_{\text{env}}/(B_m^2/8\pi)$ and $p_{\text{env}} = n_{\text{env}}k_B T_{\text{env}}$.

We consider five different initial configurations. Model M1 represents a continuous jet with constant injection velocity $v_{\text{jet}} = v_0$, whereas models M2–M5 have a time dependent injection velocity of the form

$$v_{\text{jet}} = v_0(1 + \Delta v \cos(\omega t)), \quad (3)$$

where $v_0 = 1000 \text{ km s}^{-1}$ is the mean velocity of the

flow, and $\omega = 2\pi/\tau$, $\tau = 50 \text{ yr}$ and Δv are the frequency, periodicity, and amplitude of the variability, respectively. The values of B_z , Δv and jet maximum velocity $v_{\text{max}} = v_0(1 + \Delta v)$ for the different models are given in Table 1. With these values, v_{jet} is in the range of $\sim 600 - 1400 \text{ km s}^{-1}$, as observed in HH80-81 (Martí et al. 1995, 1998).

We have also explored the case of a dense and slow jet (model M6). This model has the same parameters as the model M4, except that $v_0 = 300 \text{ km s}^{-1}$, $\Delta v = 0.3$, and the density of the jet and the surrounding medium are 1000 and 100 cm^{-3} , respectively (see Table 1).

2.2. Synthetic emission maps

2.2.1. Non-thermal radio emission and Stokes parameters

In this section, we present a brief description of the strategy used to compute the non-thermal synchrotron emission and the Stokes parameters. For details of the method we refer the reader to Ghisellini (2013). See also Rybicki & Lightman (1986) for an in-depth description of synchrotron emission.

Synchrotron emission in YSO jets is produced by relativistic electrons accelerated in internal and termination shocks (see Section 3.1). In the present study, we assume that there is a population of relativistic electrons with power-law energy distribution:

$$n_e = K \gamma_e^{-p}, \quad (4)$$

for $\gamma_{\text{min}} \leq \gamma_e \leq \gamma_{\text{max}}$ (being γ_e the Lorentz's factor), and $n_e = 0$ otherwise. We fix $p = 2.1$ in our calculations and determine K and γ_{min} assuming that the number density of non-thermal electrons is a fraction χ_n (< 1) of n_g , the electron density of the gas (assuming as well that the plasma is composed by the same number of electrons and protons, i.e. fully ionized hydrogen, in post-shocked regions):

$$\chi_n n_g = \int_{\gamma_{\text{min}}}^{\gamma_{\text{max}}} K \gamma_e^{-p} d\gamma_e \sim K \frac{\gamma_{\text{min}}^{-p+1}}{p-1}, \quad (5)$$

and that the energy density is a fraction χ_ϵ (< 1) of the gas kinetic energy density $\epsilon = m_p n_g v_g^2/2$:

$$\chi_\epsilon \epsilon = \int_{\gamma_{\text{min}}}^{\gamma_{\text{max}}} K \gamma_e^{-p} (\gamma_e - 1) m_e c^2 d\gamma_e \sim K \frac{\gamma_{\text{min}}^{-p+2}}{p-2}, \quad (6)$$

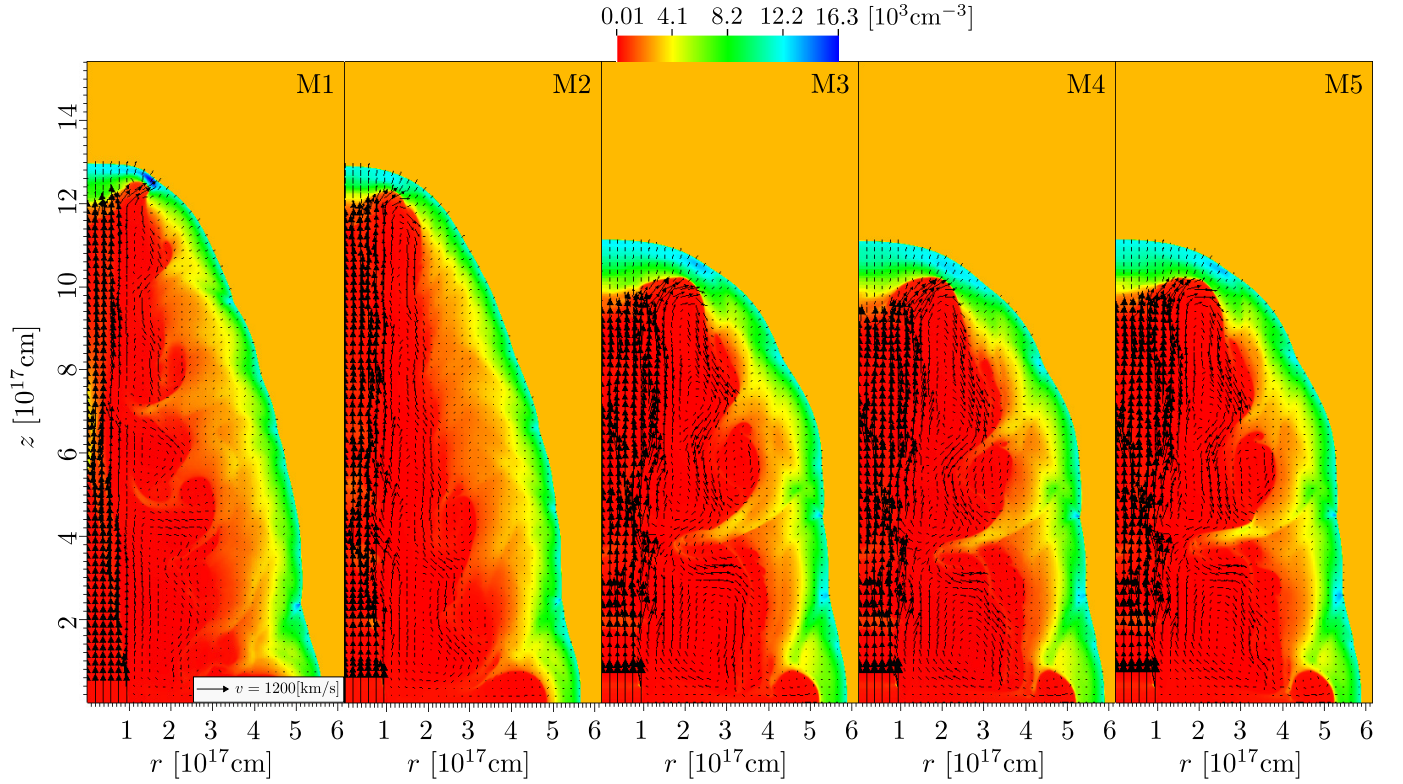


FIG. 2.— Number density stratification maps, in units of 10^3 cm^{-3} , and displayed in linear color scale (see colorbar at the top). The black arrows depict the velocity field, with a scale shown at the bottom of the leftmost panel. The integration time is $t = 1500 \text{ yr}$ in all models.

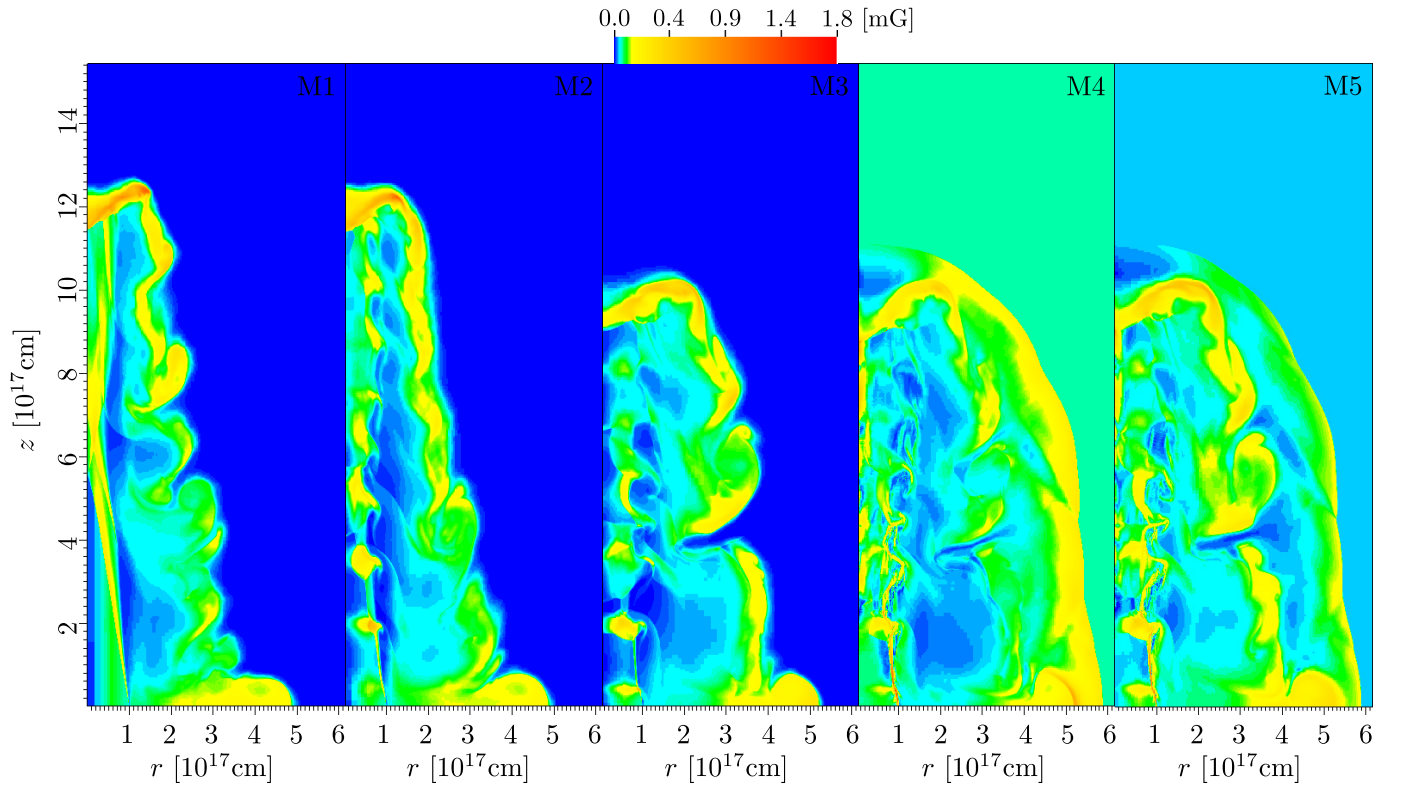


FIG. 3.— Maps of the magnetic field intensity, (see colorbar at the top for the scale, in units of mG) obtained for all models at an integration time of 1500 yr .

TABLE 1
INITIAL SETUP

Model	B_z [mG]	B_m [mG]	$n_{\text{env}}/n_{\text{jet}}$	Δv	v_{max} [km s ⁻¹]
M1	0	0.1	10	0	1000
M2	0	0.1	10	0.2	1200
M3	0	0.1	10	0.4	1400
M4	$0.1/\sqrt{2}$	$0.1/\sqrt{2}$	10	0.4	1400
M5	$0.1/\sqrt{10}$	$0.3/\sqrt{10}$	10	0.4	1400
M6	$0.1/\sqrt{2}$	$0.1/\sqrt{2}$	0.1	0.3	390

where m_e is the rest mass of the electron and c is the speed of light. From equations (5) and (6), we obtain

$$\gamma_{\min} = \frac{p-1}{p-2} \frac{\chi_e \epsilon}{\chi_n n_g} \quad (7)$$

and

$$K = (p-1) \chi_n n_g \gamma_{\min}^{p-1}. \quad (8)$$

We are interested in the study of the synchrotron radiation at frequencies $\nu \sim 1$ GHz. This emission is optically thin at frequencies larger than the self-absorption frequency (equation 4.56 of [Ghisellini 2013](#))

$$\nu_{\text{sa}} = \nu_L \left[\frac{\pi^{3/2} e R K}{4B} f_\alpha(p) \right]^{2/(p+4)} \quad (9)$$

where $\nu_L = eB/(2\pi m_e c)$ is the Larmor frequency, e is the charge of the electron, and (equation 4.52 of [Ghisellini 2013](#)):

$$f_\alpha(p) \simeq 3^{\frac{p+1}{2}} \left(\frac{1.8}{p^{0.7}} + \frac{p^2}{40} \right). \quad (10)$$

By setting $R = 10^{17}$ cm as the size of the emitting region, we obtain $\nu_{\text{sa}} \simeq 3$ MHz $\ll 1$ GHz for typical values of density and velocity in our simulations.

In the optically thin case, the synchrotron specific intensity, for the isotropic case, can be written as (see equation 4.45 [Ghisellini 2013](#)):

$$j_s(\nu) = \frac{3}{16} \frac{\sigma_T c K u_B}{\sqrt{\pi} \nu_L} f_j(p) \left(\frac{\nu}{\nu_L} \right)^{(1-p)/2} \quad (11)$$

where $\sigma_T = 6.65 \times 10^{-25}$ cm² is the Thomson cross section, $u_B = B^2/(8\pi)$ is the magnetic energy density, and

$$f_j(p) \simeq 3^{p/2} (2.25/p^{2.2} + 0.105) \quad (12)$$

(see equation 4.46 [Ghisellini 2013](#)). Using equations (7) and (8), equation (11) gives:

$$j_s(\nu) = K_s \chi_n^{1-2\alpha} \chi_e^{2\alpha} n_g v_g^{4\alpha} B_\perp^{\alpha+1} \nu^{-\alpha}, \quad (13)$$

where B_\perp is the component of the magnetic field perpendicular to the line of sight (LoS) and $\alpha = (p-1)/2 = 0.55$ is the spectral index. The factor K_s in equation (13) is:

$$K_s = K_1 K_2 m_e^{1-3\alpha} c^{2-5\alpha} (\mu m_H)^{2\alpha} f_j(p) \quad (14)$$

where μ is the molecular weight and m_H is the proton rest mass. The factors K_1 and K_2 are

$$K_1 = (p-1) \left(\frac{p-2}{p-1} \right)^{(p-1)} \quad (15)$$

and

$$K_2 = \frac{3}{2^{7-3\alpha}} \sigma_T (\pi e)^{(2\alpha-1)/2}. \quad (16)$$

Synthetic synchrotron intensity maps are obtained from our 2D simulation in the following way. For each cell of our 2D axisymmetric grid we compute the synchrotron emissivity. The 2D plane of simulation (rz -plane) is tilted with respect to the plane of the sky (around the x' -axis) by an angle φ , and it is revolved around the symmetry axis (z), sampling a large number of angles in the θ direction in order to obtain a ‘‘3D distribution’’ of the synchrotron emissivity. Then, the emissivity $j_s(\nu)$ is

integrated along the LoS ($I(\nu) = \int_{\text{LoS}} j_s(\nu) dy'$), which was chosen to be y' (see Figure 1). In this study, a dependence with the angle between the shock normal and the post-shocked magnetic field is not considered (see for instance [Orlando et al. 2007](#); [Petruk et al. 2009](#); [Schneiter et al. 2015](#) for a discussion of the acceleration mechanisms in supernova remnants).

From the synchrotron emission we have also carried a polarization study by means of maps of the Stokes parameters Q_B and U_B , which can be computed as:

$$Q_B(x', z', \nu) = \int_{\text{LoS}} f_0 j_s(\nu) \cos[2\phi(y')] dy', \quad (17)$$

$$U_B(x', z', \nu) = \int_{\text{LoS}} f_0 j_s(\nu) \sin[2\phi(y')] dy', \quad (18)$$

(see e.g. [Clarke et al. 1989](#); [Jun & Norman 1996](#)), where (x', z' are the coordinates in the plane of the sky (see Figure 1, dy' is measured along the LoS, $\phi(y')$ is the position angle of the local magnetic field on the plane of the sky, and

$$f_0 = \frac{\alpha + 1}{\alpha + 5/3} \quad (19)$$

is the degree of linear polarization. The intensity of the linearly polarized emission is given by

$$I_P(x', z', \nu) = \sqrt{Q_B^2(x', z', \nu) + U_B^2(x', z', \nu)} \quad (20)$$

and the map of the position angle of the magnetic field (which gives the orientation of the magnetic field in the plane of the sky) is computed as

$$\chi_B(x', z') = \frac{1}{2} \tan^{-1}(U_B(x', z', \nu)/Q_B(x', z', \nu)). \quad (21)$$

2.2.2. Thermal X-ray emission

We calculated the thermal emission by integrating the free-free emissivity $j_\nu(n_g, T)$ along the LoS. In the low density regime, $j_\nu(n_g, T) = n_g^2 \Lambda(T)$, where n_g is the electron density and T is the temperature. As with non-thermal radio emission, we assume that the post-shocked medium is fully ionized. The function $\Lambda(T)$ was constructed with the CHIANTI atomic database ([Dere et al. 1998](#)) considering the energy range [0.15-8] keV and assuming solar metallicity.

3. RESULTS

The numerical simulations with the initial conditions summarized in Table 1 were carried out until they reach an integration time of 1500 yr.

3.1. Shocks in protostellar jets

Figure 2 displays the number density stratification and the velocity field. As the jet interacts with the surrounding medium, it forms a double shock structure, where the environment gas is accelerated by a forward shock, and the jet plasma is decelerated by a reverse shock. This structure, as well as the contact discontinuity separating the shocked interstellar material from the shocked jet material, is clearly visible at the head of the jet shown in Figure 2. In all cases, a slow bowshock travels against the surrounding environment with velocities $\sim [200-260]$ km s⁻¹.

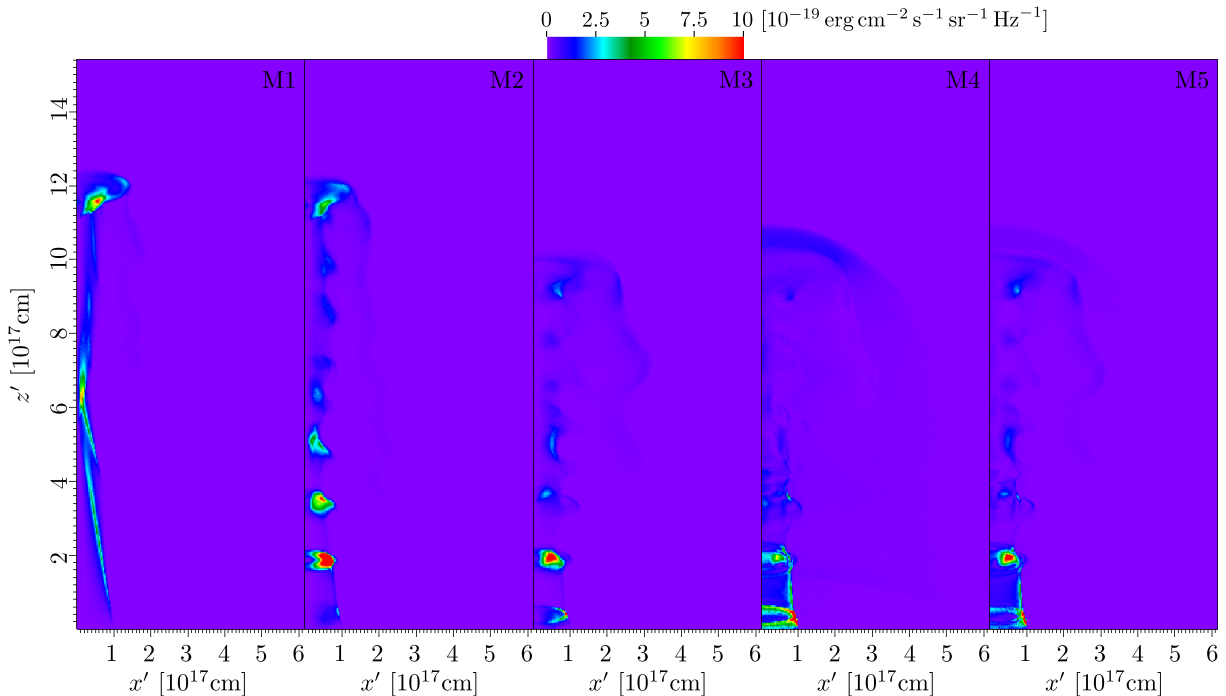


FIG. 4.— Comparison of synthetic maps of the intensity of the linearly polarized radio emission obtained for all models at $\nu = 5$ GHz.

Internal shocks are present only in the models where $\Delta v \neq 0$. Several jumps in axial velocity are present which mark the position of the internal shocks and have values in the range $[400 - 500]$ km s^{-1} . With these values and the Rankine-Hugoniot jump conditions, we can estimate internal shocks velocities as large as 1000 km s^{-1} . These velocities, and considering that these shocks move in a low density medium, with densities of the order of 200 cm^{-3} imply that the internal shocks are adiabatic⁶. Note that in models M3–M5 ($\Delta v = 0.4$) the bow shock is significantly slower (200 km s^{-1}) than in models M1 and M2 (260 km s^{-1}).

Figure 3 displays the magnitude of the magnetic field B . In models M2 and M3 the jet variability is quite evident by the presence of a thin Mach disk in several internal working surfaces. In contrast, the map corresponding to model M4 and M5 have a more complex morphology with less defined working surfaces, and a larger cocoon structure due to the magnetic field along the symmetry axis.

3.2. Radio polarization

Figure 4 shows synthetic maps of the intensity of the linearly polarized radio emission I_P , at 5 GHz, for all models. The spatial resolution of these maps is 10^{-3} pc. We have considered that the jet axis is tilted 15° with respect to the plane of the sky.

In model M1 ($\Delta v = 0$) the jet develops a single radio knot associated with material within the Mach disk (see Figure 4, left panel). The extended feature observed at $z' \sim 6 \times 10^{17} \text{ cm}$, associated with an internal shock, is an artifact produced by the reflective boundary condition imposed along the symmetry axis.

⁶ The cooling distance (see e.g. the equation (6) of Raga et al. 2002) results larger than the jet radius, implying an adiabatic nature for the internal shocks.

In contrast, the other models ($\Delta v \neq 0$) display knotty radio structures produced by the internal shocks⁷. These knots decrease in brightness with distance from the jet source. Model M4 ($B_z = B_m$) also shows radio emission in the region behind the main bow shock. The radio emission of this region in model M5, which has $B_z = B_m/3$ (see Table 1), results in a lower emission compared with model M4.

In Figure 5 the degree of polarization of the synchrotron radiation ($I_P(x', z', \nu)/I(x', z', \nu)$) shows an important result. Models M1–M3 exhibit a high degree of polarization of the synchrotron emission while model M4 displays strong variations toward the symmetry axis. This behavior is also observed in model M5, although to a lesser degree. These results can be understood considering that, in an helical magnetic field, emission from regions with linearly polarized synchrotron radiation whose polarization directions are orthogonal to each other cancel out when the emission is integrated along a LoS nearly perpendicular to the axis of symmetry of jet. A decrease of the degree of polarization has been observed in the jet associated with HH 80–81 (Carrasco-González et al. 2010).

Figure 6 displays maps of the distribution of the position angle of the magnetic field $\chi_B(x', z')$. As in observational studies, these $\chi_B(x', z')$'s maps were performed from the synthetic maps of the Stokes parameters Q_B and U_B , by using of equations (17), (18), and (21). These maps show that for models M4 and M5, which display variations in the degree of polarization, the orientation of the magnetic field in the plane of the sky has a compo-

⁷ We are considering a jet with a fixed axis, and thus the working surfaces move along the axis of symmetry of the jet and never exit the cocoon carved by the main bow shock. Thus, their interaction is with the previously ejected jet material and not with the external medium.

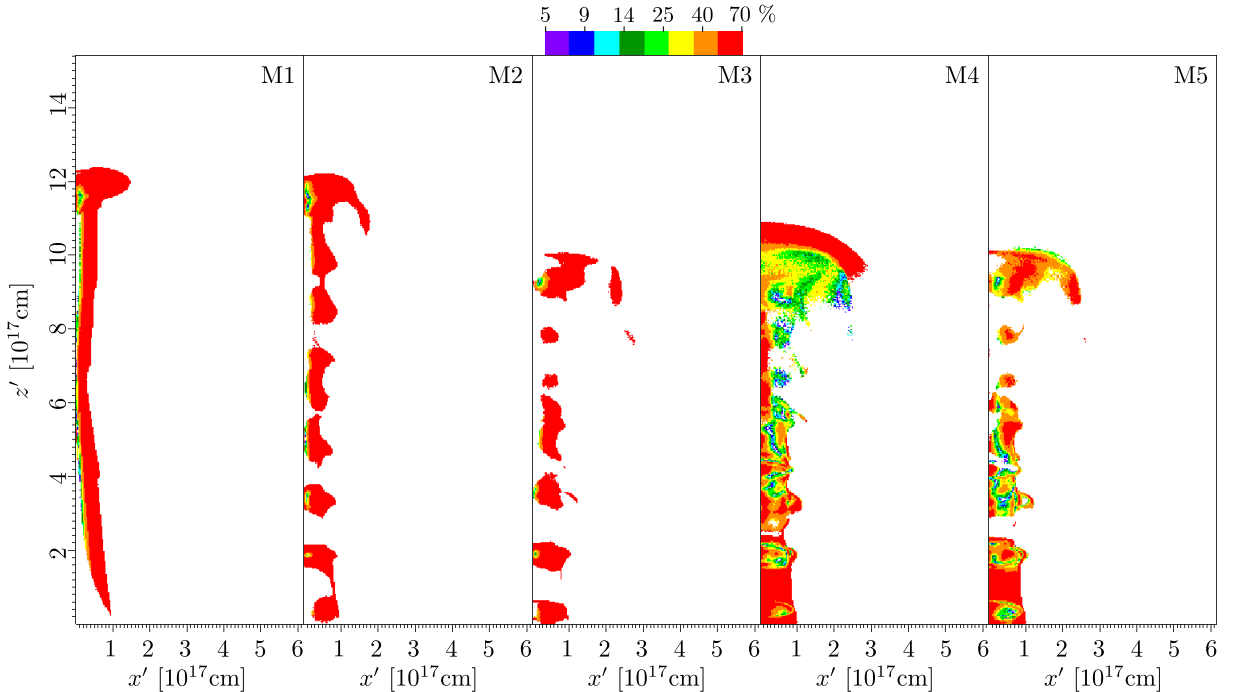


FIG. 5.— Same as Figure 4 but displaying maps of degree of polarization

ment parallel to the symmetry axis (given an additional support of the helical nature of the magnetic field), while in models M1-M3 the magnetic field is mostly perpendicular to it.

A comparison between synchrotron and thermal X-ray emission for models M3 and M4 is shown in Figure 7. For both models, the X-ray emission maps also display a knotty structure although less defined than its radio counterpart. Most of the thermal X-ray emission comes from the environment material swept up by the main bow shock, as shown by Bonito et al. (2004, 2007, 2010) in hydrodynamic simulations. As it was mentioned above for the map of the linearly polarized intensity, the total synchrotron emission maps display bright knots close to the central source. These bright knots emit a radio flux, at 5 GHz, of the order of $1.5\chi_n^{1-2\alpha}\chi_\epsilon^{2\alpha} \times 10^{-18}\text{erg s}^{-1}\text{sr}^{-1}\text{cm}^{-2}\text{Hz}^{-1}$, which is (aside of setting the exact value for the fractions χ_n and χ_ϵ) in reasonable agreement with the flux reported by Carrasco-González et al. (2010) for the knots in HH 80-81 (1 mJy/beam or $10^{-18}\text{erg s}^{-1}\text{sr}^{-1}\text{cm}^{-2}\text{Hz}^{-1}$).

Figure 8 shows that the synchrotron emission for the case of a dense and slow jet (model M6) is 30 times lower than the emission for a lighter and faster jet (model M4). Furthermore, it is important to do a comparison of the magnitude obtained for both the non-thermal and thermal emission mechanisms in radio wavelengths. The thermal radio-continuum emission is optically thin for the parameters chosen in our simulations⁸. Therefore, one can compute the ratio of non-thermal to thermal emissivities (using equation (5) of Velázquez et al. (2007) and equation (11) of this paper) in the bright radio knots of models M4 and M6 (located at $z' \simeq 1.8 \times 10^{17}$ cm and $z' \simeq 0.5 \times 10^{17}$, respectively). For model M6 this ratio is

$j_s(\nu)/j_{\text{th}}(\nu) = 0.03$ at a frequency $\nu = 5$ GHz, while for model M4 the ratio is 1.4. Thus, a dense and slow jet does produce synchrotron emission, however at a level that is negligible compared to the thermal radio-continuum.

4. DISCUSSION AND CONCLUSIONS

Carrasco-González et al. (2010) have shown the existence of polarized radio emission associated with the HH 80-81 protostellar jet. However, this issue has not been studied by HD or MHD simulations. We present the results obtained from 2.5D MHD simulations of low- and high-density YSO jets. We have considered cases with a constant, and a time-dependent jet ejection velocity. Furthermore, cases in which the magnetic field is toroidal or helical were analyzed.

Assuming a population of relativistic electrons which are accelerated within stellar shock jets, we have used standard prescriptions to estimate their synchrotron emission. Our results indicate that while the thermal X-ray emission is dominated by the shocked environment material at the head of the jet (in agreement with Raga et al. 2002; Bonito et al. 2004, 2007, 2010), the non-thermal radio emission turns out to be dominated by the jet material inside the internal shocks.

Also, radio maps reveal that the variability in jet velocity is important in generating bright knots of synchrotron emission, produced when slow jet material is caught up by faster jet material.

Our models show that a jet with a toroidal magnetic field emits synchrotron radiation with a high degree of polarization. In contrast, models with a helical magnetic field exhibit a decrease on the degree of polarization, in good agreement with observational results (Carrasco-González et al. 2010).

Finally, our results indicate that non-negligible synchrotron emission can be obtained in low-density and high-velocity protostellar jets.

⁸ The opacity τ_{th} is $\ll 1$, considering the equation (3) of Velázquez et al. (2007).

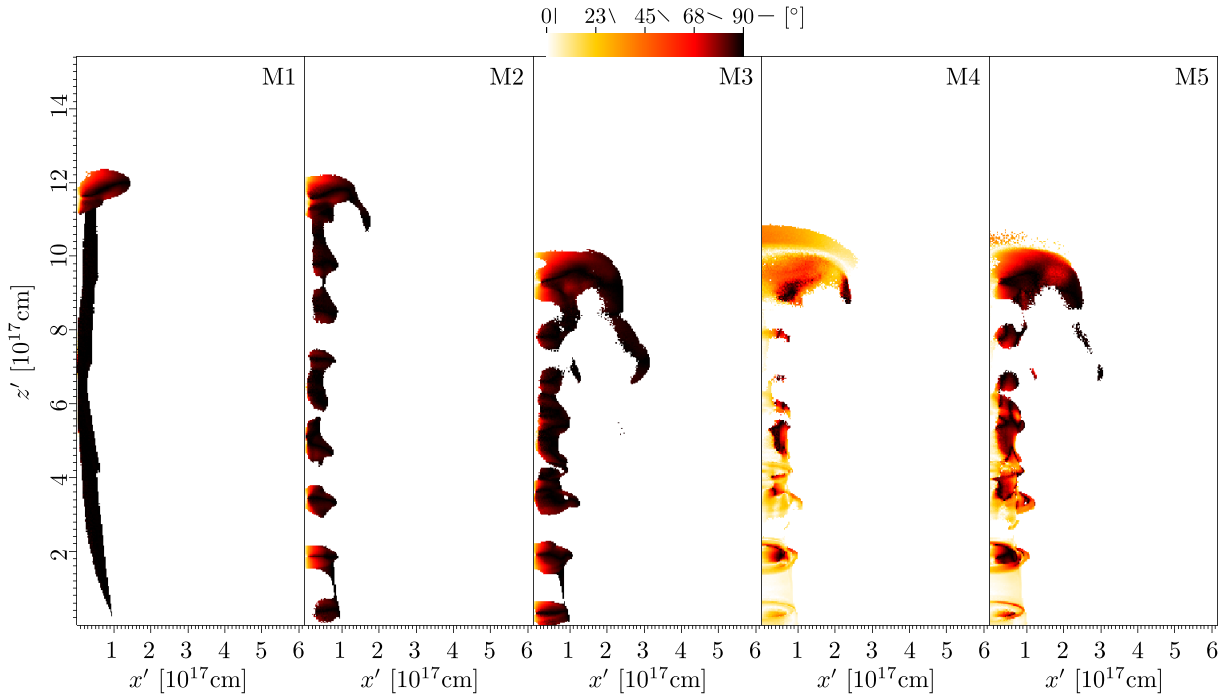


FIG. 6.— Same as Figure 4 but showing the position angle of the magnetic field B (which is measured with respect to the z' -axis, as indicated by the stick marks in the colorbar).

We thank the anonymous referee for her/his very useful comments, with help us to improve the previous version of this manuscript. MC, PFV, FdC, and AE thank financial support from CONACyT grants 167611 and 167625, CONICET-CONACyT grant CAR 190489, and DGAPA-PAPIIT (UNAM) grants IG 100214, IA 103115, IA 109715, IA 103315. A.T.A. acknowledges support from the UK Science and Technology Facilities Council under grant number ST/K00106X/1. C.C-G. ac-

knowledges support by DGAPA-PAPIIT (UNAM) grant number IA 101214. LFR acknowledges support from CONACyT and DGAPA-PAPIIT (UNAM) grants. We also thank Enrique Palacios for maintaining the Linux Server on which the simulations were carried out. PFV dedicates this work to the memory of Jesús Francisco García Cosío, María Guadalupe Gudelia Roldán, and María Norma Brito.

REFERENCES

- Araudo, A. T., & Rodríguez, L. F. 2012, in American Institute of Physics Conference Series, Vol. 1505, American Institute of Physics Conference Series, ed. F. A. Aharonian, W. Hofmann, & F. M. Rieger, 281–284
- Blandford, R. D., & Payne, D. G. 1982, *MNRAS*, 199, 883
- Bonito, R., Orlando, S., Miceli, M., Eisloffel, J., Peres, G., & Favata, F. 2010, *A&A*, 517, A68
- Bonito, R., Orlando, S., Peres, G., Favata, F., & Rosner, R. 2004, *A&A*, 424, L1
- . 2007, *A&A*, 462, 645
- Broderick, A. E., & McKinney, J. C. 2010, *ApJ*, 725, 750
- Carrasco-González, C., Rodríguez, L. F., Anglada, G., Martí, J., Torrelles, J. M., & Osorio, M. 2010, *Science*, 330, 1209
- Clarke, D. A., Burns, J. O., & Norman, M. L. 1989, *ApJ*, 342, 700
- Curran, R. L., & Chrysostomou, A. 2007, *MNRAS*, 382, 699
- De Colle, F., & Raga, A. C. 2006, *A&A*, 449, 1061
- De Colle, F., Raga, A. C., & Esquivel, A. 2008, *ApJ*, 689, 302
- De Colle, F., Ramirez-Ruiz, E., Granot, J., & Lopez-Camara, D. 2012, *ApJ*, 751, 57
- Del Zanna, L., Volpi, D., Amato, E., & Bucciantini, N. 2006, *A&A*, 453, 621
- Dere, K. P., Landi, E., Mason, H. E., Fossi, B. C. M., & Young, P. R. 1998, in *Astronomical Society of the Pacific Conference Series*, Vol. 143, *The Scientific Impact of the Goddard High Resolution Spectrograph*, ed. J. C. Brandt, T. B. Ake, & C. C. Petersen, 390
- Garay, G., Brooks, K. J., Mardones, D., & Norris, R. P. 2003, *ApJ*, 587, 739
- Garay, G., Ramirez, S., Rodriguez, L. F., Curiel, S., & Torrelles, J. M. 1996, *ApJ*, 459, 193
- Ghisellini, G. 2013, *Radiative Processes in High Energy Astrophysics* (Springer)
- Goldston, J. E., Quataert, E., & Igumenshchev, I. V. 2005, *ApJ*, 621, 785
- Gómez, J. L., Marscher, A. P., Jorstad, S. G., Agudo, I., & Roca-Sogorb, M. 2008, *ApJ*, 681, L69
- Jun, B.-I., & Norman, M. L. 1996, *ApJ*, 472, 245
- Laing, R. A., Canvin, J. R., Bridle, A. H., & Hardcastle, M. J. 2006, *MNRAS*, 372, 510
- Lind, K. R., Payne, D. G., Meier, D. L., & Blandford, R. D. 1989, *ApJ*, 344, 89
- Martí, J., Rodríguez, L. F., & Reipurth, B. 1995, *ApJ*, 449, 184
- . 1998, *ApJ*, 502, 337
- Masciadri, E., Velázquez, P. F., Raga, A. C., Cantó, J., & Noriega-Crespo, A. 2002, *ApJ*, 573, 260
- Orlando, S., Bocchino, F., Reale, F., Peres, G., & Petruk, O. 2007, *A&A*, 470, 927
- Petruk, O., Dubner, G., Castelletti, G., Bocchino, F., Iakubovskiy, D., Kirsch, M. G. F., Miceli, M., Orlando, S., & Telezhinsky, I. 2009, *MNRAS*, 393, 1034
- Porth, O., Fendt, C., Meliani, Z., & Vaidya, B. 2011, *ApJ*, 737, 42
- Raga, A., & Noriega-Crespo, A. 1998, *AJ*, 116, 2943
- Raga, A. C., Noriega-Crespo, A., & Velázquez, P. F. 2002, *ApJ*, 576, L149
- Rodriguez, L. F., Curiel, S., Moran, J. M., Mirabel, I. F., Roth, M., & Garay, G. 1989, *ApJ*, 346, L85
- Rybicki, G. B., & Lightman, A. P. 1986, *Radiative Processes in Astrophysics*
- Schneider, E. M., Velázquez, P. F., Reynoso, E. M., Esquivel, A., & De Colle, F. 2015, *MNRAS*, 449, 88

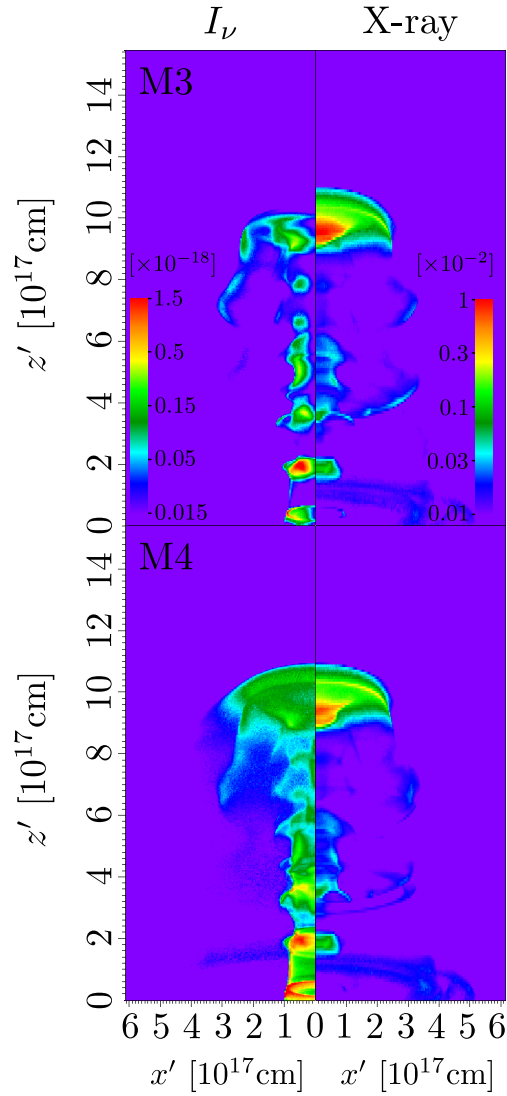


FIG. 7.— Comparison of synthetic synchrotron emission maps at $\nu = 5$ GHz (left panels) with thermal X-ray emission maps (right panels) for models M3 and M4 (upper and bottom panels, respectively). The synchrotron emission is given in units of $\chi_n^{1-2\alpha} \chi_\epsilon^{2\alpha} [\text{erg cm}^{-2} \text{s}^{-1} \text{sr}^{-1} \text{Hz}^{-1}]$, while the thermal X-ray emission is in units of $\text{erg cm}^{-2} \text{s}^{-1} \text{sr}^{-1}$.

Tregillis, I. L., Jones, T. W., & Ryu, D. 2001, ApJ, 557, 475

Velázquez, P. F., Gómez, Y., Esquivel, A., & Raga, A. C. 2007, MNRAS, 382, 1965

Volpi, D., Del Zanna, L., Amato, E., & Bucciantini, N. 2008, A&A, 485, 337

Wilner, D. J., Reid, M. J., & Menten, K. M. 1999, ApJ, 513, 775

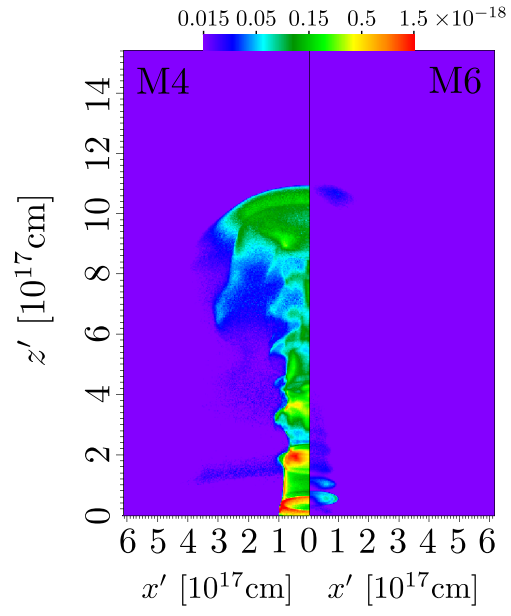


FIG. 8.— Comparison of synthetic synchrotron emission maps, at 5 GHz, of model M4 (left panel) with model M6 (right panel). The synchrotron emission is given in units of $\chi_n^{1-2\alpha}\chi_e^{2\alpha}$ [erg cm⁻² s⁻¹ sr⁻¹ Hz⁻¹].